Toughening of unmodified polyvinylchloride through the addition of nanoparticulate calcium carbonate

I. Kemal [a,b], A. Whittle [c], R. Burford [b], T. Vodenitcharova [a], M. Hoffman [a,*]

[a] School of Materials Science and Engineering, University of New South Wales, Sydney, NSW 2052, Australia
[b] School of Chemical Sciences and Engineering, University of New South Wales, Sydney, NSW 2052, Australia
[c] IPLEX Pipelines Australia Pty Ltd., 35 Alfred Road, Chipping Norton, NSW 2170, Australia

ARTICLE INFO

ABSTRACT

PVC/CaCO$_3$ polymer nanocomposites of differing compositions were produced using a two-roll mill and compression molding. The morphology was observed using transmission electron microscopy, and the static and dynamic mechanical and fracture properties determined. The presence of nanometer-sized CaCO$_3$ particles led to a slight decrease in the tensile strength but improved the impact energy, the storage modulus and the fracture toughness. Fracture surface examination by scanning electron microscopy indicated that the enhanced fracture properties in the nanocomposites were caused by the assisted void formation at the particles. This hypothesis is supported by a microstructure-based finite element modeling based upon elastic–plastic deformation around a weakly bonded particle. Hence, this provides an explanation of both the uniaxial tensile behavior and enhanced toughness of the nanocomposites.

© 2009 Elsevier Ltd. All rights reserved.

1. Introduction

The use of inorganic fillers has been practiced for many decades in both elastomers and plastic materials. In regard to elastomers, the key aim is either to provide a major reinforcement, for example in synthetic elastomers using carbon black and silica, or to cheapen the compounds using clay and other materials [1].

For thermoplastics like PVC, the latter aim is often achieved by using cheap fillers to stiffen the material or control the acoustic properties [2]. In engineering applications where a combination of stiffness and toughness is desired, such as for PVC pipes, large quantities of inorganic fillers are usually avoided [3]. However, there is an increasing awareness of possibilities to simultaneously improve a broad range of mechanical properties and reduce costs by incorporating nanometer-sized particles [4–7].

Conventionally, the toughness of rigid unplasticized PVC (u-PVC) can be improved by using an impact modifier of rubbery particles, such as chlorinated polyethylene (CPE) or acrylonitrile butadiene styrene (ABS) to make what is known as modified PVC (m-PVC). The increase in toughness can be attributed to cavity formation in the rubbery particles when stress is applied, thus deforming the matrix through the formation of shear bands or crazes which can absorb energy [8]. Despite excellent toughening effects, the presence of rubbery particles decreases the modulus and yield strength, and can increase cost.

Ground calcium carbonate of particle size greater than 1 μm is often added to PVC compounds to reduce cost, but at the expense of performance through reduction in tensile and impact strength [2,9,10]. However, it has been found that the addition of nanometer-sized calcium carbonate (nano-CaCO$_3$) significantly improves both the toughness and stiffness of PVC, while having little effect on the tensile strength [11,12]. The recent development of techniques for cheap processing of nano-CaCO$_3$ means that this new process has potential applications in commodity applications of PVC such as piping materials.

The question at hand, however, is to ascertain the mechanism whereby nanoparticles lead to enhanced toughness. For a polymer matrix with rigid inorganic particles, an improvement in modulus is expected according to conventional rules of mixing. On the other hand, toughening by micron-sized inorganic particles can generally be explained by a crack pinning mechanism [13] and/or crack deflection theory [14]. However, the application of these theories to nanometer-sized particles does not predict a toughness enhancement in PVC as the nanoparticles may be too small to effectively interact with the propagating crack [15].

When designing both materials and components, it is necessary to ascertain the true fracture toughness of a material. In the field of plastics, toughness is often measured using Charpy and Izod impact

* Corresponding author. Tel.: +61 2 9385 4432; fax: +61 2 9385 5956.
E-mail address: m.hoffman@unsw.edu.au (M. Hoffman).

tests due to their simplicity. However, the results of these tests depend upon specimen geometry. Although, results are expressed as energy absorbed per unit area or energy absorbed per specimen width, they are known to vary non-proportionally with these dimensions. Hence, impact toughness cannot be utilized as an intrinsic measure of a material property for use in component or material design due to the size-dependent deformation processes [16]. However, a method for the determination of fracture toughness has been developed by Marshall et al. [16] and Brown [17], which measures the strain energy release rate G_c directly from the results of impact tests on multiple specimens with different notch depths. The method was further extended by Plati and Williams [18] who examined a range of plastic materials, including PVC. This method was then adopted as part of a U.K. Water Industry specification [19] and as an ESIS protocol [20] for polyethylene and PVC pipes. The critical strain energy release rate, G_c, test method has been successfully used to measure the fracture toughness of both u-PVC and m-PVC by Whittle et al. [21]. The G_c test has shown an increasing fracture toughness with increasing CPE volume fraction in m-PVC. Typical fracture toughness values of 2.7 kJ/m^2 for u-PVC and 4.9 kJ/m^2 for m-PVC with 6 phr CPE were found under high loading rate conditions.

In this study, we seek to ascertain the deformation mechanisms associated with the increase in toughness and stiffness as a result of the inclusion of inorganic nanoparticles in a PVC matrix. Consideration was also made of the effect of these deformation processes upon strength. The results obtained were compared with the use of impact modifiers for toughness enhancement. PVC nanocomposites with differing nano-CaCO$_3$ levels were processed by a melt blending method and the fracture toughness, dynamic moduli and strength, obtained. Microstructures were determined using transmission electron microscopy and the extensive fracture surface analysis utilized to elucidate the deformation mechanisms. A mechanistic deformation model was then constructed to explain the effect of microstructure upon strength and fracture toughness.

2. Experimental procedures

2.1. Material processing

Commercial-grade raw materials consisting of PVC resins (K57, Australian Vinyls), Ca–Zn-based thermal stabilizers (CP 1009, Chemson Pacific) and lubricants (L4000, Chemson Pacific) were combined with 3, 6, 9, 12 and 20 parts per hundred of resin (phr) by weight of nanoparticle calcium carbonate (NPCC, Singapore Nano Material Technology) in a dry blend. A monolithic sample containing no NPCC was also manufactured along with a reference m-PVC, which contains 6 phr of CPE rubbery particles. Dry powder blends were produced in a 2-L Papenmeier mixer heated from room temperature to 120 °C over approximately 15 min followed by cool mixing at room temperature for 2 min. Dry blends were processed using a two-roll mill operating at equal roll speeds and a temperature of 160 °C. The resulting compounds were cooled and granulated into flakes using a bench-top mechanical granulator. The flakes were then molded into rectangular sheets by compression molding at 185 °C and 2 MPa pressure for 5 min using a Carver type press.

2.2. Microstructural characterisation

The calcium carbonate nanoparticle was characterized by TEM and the ImageJ analysis software (NIH freeware). The surface area was calculated by BET surface area measurement technique, using Micromeritics Tristar 3000 Analyser under a nitrogen environment. The particles were pretreated at 150 °C under vacuum to remove moistures prior to BET measurement.

The composite morphology was examined using a JEOL 1400 TEM at an accelerating voltage of 75 kV. Samples were prepared using a Reichert Jung ultra-microtome equipped with a diamond knife to cut films of 80–100 nm thickness at room temperature. The cut sections were placed on a formvar-coated copper grid for observation in the TEM. Fracture surface examination following mechanical testing was undertaken using a JEOL S900 field emission scanning electron microscope (FESEM). Samples were coated with chromium prior to observation. The crack process zone under the impact fracture surface was also examined by FESEM. A cross-section perpendicular to the fracture plane was cut in the centre along the notch. The surface was trimmed by ultra-microtome and coated with chromium prior to observation by SEM.

2.3. Mechanical property testing

Six tensile dumbbell specimens conforming to type 1 ISO R527:1966 [22] of each composition were machined from each compression-molded slab using a pantograph cutting tool. To determine the yield stress, tensile testing was carried out according to AS1145.1-2001 [23] using an Instron model 1185 universal tensile testing machine at an extension rate of 10 mm/min. The gauge length extension was measured using a laser extensometer. Dynamic mechanical analysis (DMA) was undertaken from room temperature to 135 °C using a TA Instruments DMA Q800, cycling at 5 μm amplitude and 1 Hz frequency. The samples (45 mm × 12 mm × 5 mm) were cut from the compression-molded slab. A three point bending mode with a dual cantilever configuration was used.
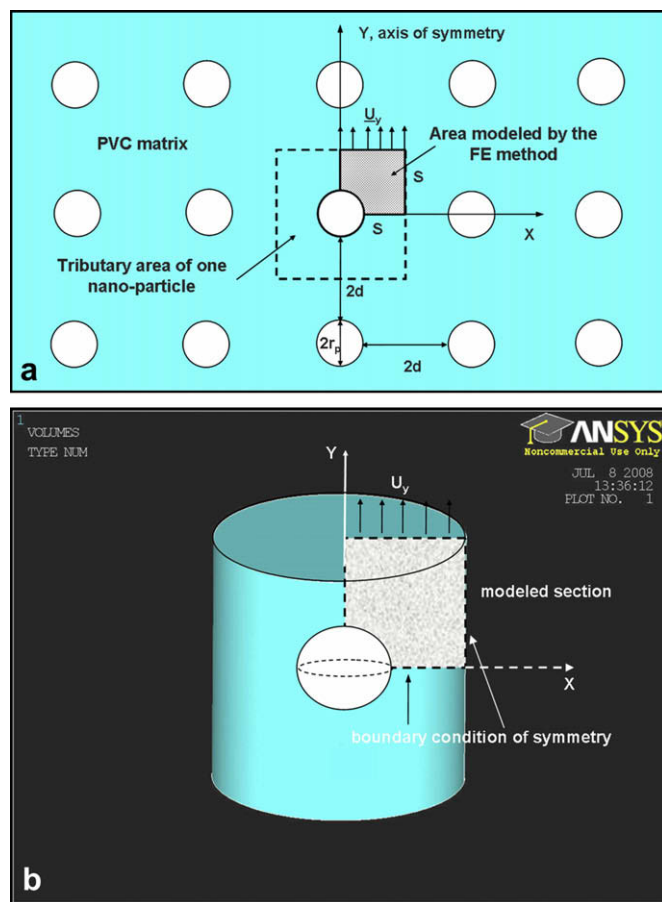
Fig. 1. (a) Schematic of the FE model assuming homogeneous particles' distribution in the matrix and (b) modeled structure following application of axisymmetric constraints.
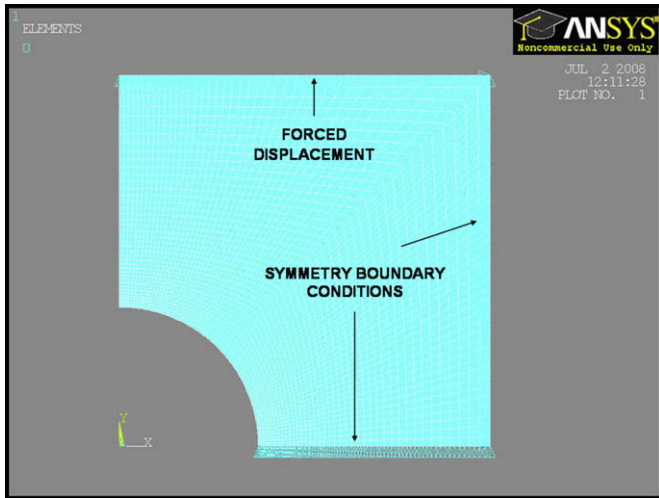
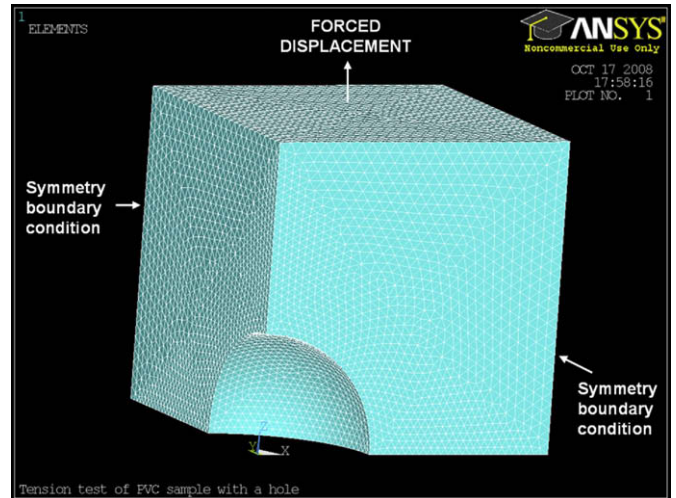**Fig. 2.** 2D FEA mesh of the matrix around the inclusion.

Fig. 4. 3D FEA mesh of the matrix around the inclusion.

Ten single-edge notched beam (SENB) impact test specimens (100 mm × 12.7 mm × 5 mm) were cut using a band saw, and notched using a multi-toothed broaching tool as described in ISO/DIS 11673.2 [24] to give a notch radius of 16 μm. Impact testing was performed according to AS1146.2-1990 [25] using a Zwick Model 5102 pendulum impact tester. For determination of fracture toughness, 22 SENB specimens (100 mm × 12.7 mm × 5 mm) with different notch depths were cut from the compression-molded slab and notched in a way similar to the impact specimens. The notches were cut to depths of ∼0.8 to 7.0 mm, and the samples were conditioned at 20 ± 2 °C in the laboratory for one day. The energy to fracture was measured on a pendulum impact tester with the support span set at 70 mm and impact velocity of 2.93 m/s. The fracture toughness was calculated according to the ESIS strain energy release rate protocol [20].

2.4. Finite element analysis

To ascertain the effect of inclusions upon the deformation process at a microstructural level a finite element model was constructed using ANSYS 11.0 finite element analysis (FEA) software. For the model, it was assumed that bonding between the particles and the matrix is very weak, to the extent that the particles can be assumed to be voids in a matrix around which a stress concentration is induced on loading. A structure in which the particles were evenly distributed through the matrix is assumed as shown in Fig. 1(a). The unit volume modeled by the FE method covers the tributary of one nanoparticle of 20, 30 and 40 nm radius. S denotes symmetry boundary conditions; $2d$ is the distance between two particles in both x- and y-direction. Strain was applied in the form of a displacement in the y-direction U_y. Axisymmetric conditions were applied as per Fig. 1(b). A comparison was made using a three-dimensional model as outlined subsequently to confirm results obtained using the axisymmetric model and revealed only a very small discrepancy. Hence, the axisymmetric model was subsequently used due to faster solve time.

The model was then meshed using quadratic 2D solid linear elements, 4 node PLANE182 (enhanced strain formulation, axisymmetric option) as shown in Fig. 2. The number of elements depends on the inter-particle distance (d). The matrix modulus was chosen to be 3500 MPa based on experimental data.

The material model was chosen of multi-linear von Mises formulation and the true tensile stress–strain curve of the u-PVC matrix was calculated from the experimental engineering stress–
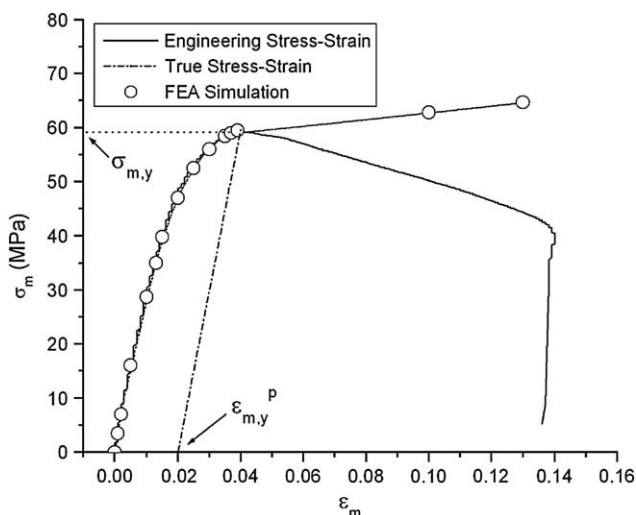

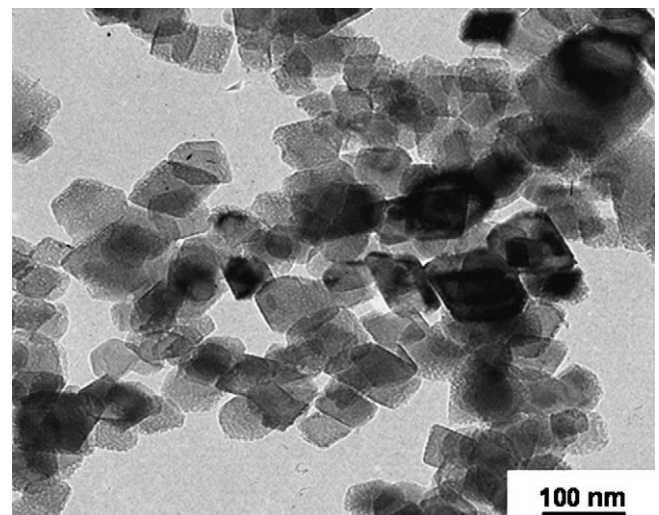**Fig. 3.** Engineering and true tensile stress–strain curve of the resin (u-PVC).

Fig. 5. TEM micrograph of the nano-CaCO$_3$ particles.

strain curve according to a method proposed by Du et al. [26] as shown in Fig. 3. From the stress–strain curve, the maximum stress ($\sigma_{m,y}$) was estimated to be 59.5 MPa, providing a 2% plastic strain ($\varepsilon_{m,y}^{p}$). The von Mises failure criterion is applied in this study, such that the composites fail under applied load when the equivalent stress (σ_{m}^{eqv}) and equivalent plastic strain ($\varepsilon_{m}^{eqv,p}$) become equal to the maximum stress ($\sigma_{m,y}$) and 2% plastic strain ($\varepsilon_{m,y}^{p}$), respectively.

The material model was introduced in the FEA software in a table format where the discrete values of stresses and strains closely follow the true stress–strain curve, represented by hollow circles in Fig. 3.

To simulate the test conditions, a strain was applied in the positive *y*-direction ($\varepsilon_{c} = (U_y/d + r_p)$) and the applied stress σ_{c} calculated as the reaction force along the *x*-axis (P) divided by the dimension $d + r_p$.

For the yield criteria it is assumed that the composite will yield when the matrix has yielded – i.e., the applied tension on the composite (σ_{c}) reaches the point of yield of the composite ($\sigma_{c,y}$) when the von Mises stress at any point in the matrix reaches the yield stress of the matrix ($\sigma_{m,y}$) or when the von Mises strain in the matrix becomes equal to the 2%.

The particle spacing (d) can be calculated based on the volume fractions (ϕ_p) and particles size (r_p) as described by Equation (1) where k is a geometric constant representing the spatial arrangement of the particles in the matrix, i.e., $k = 1$ for simple cubic lattice, $2^{1/3}$ for body-centered lattice and $4^{1/3}$ for face-centered lattice [27]:

$$d = r_p \left[k \left(\frac{\pi}{6\phi_p} \right)^{1/3} - 1 \right] \tag{1}$$
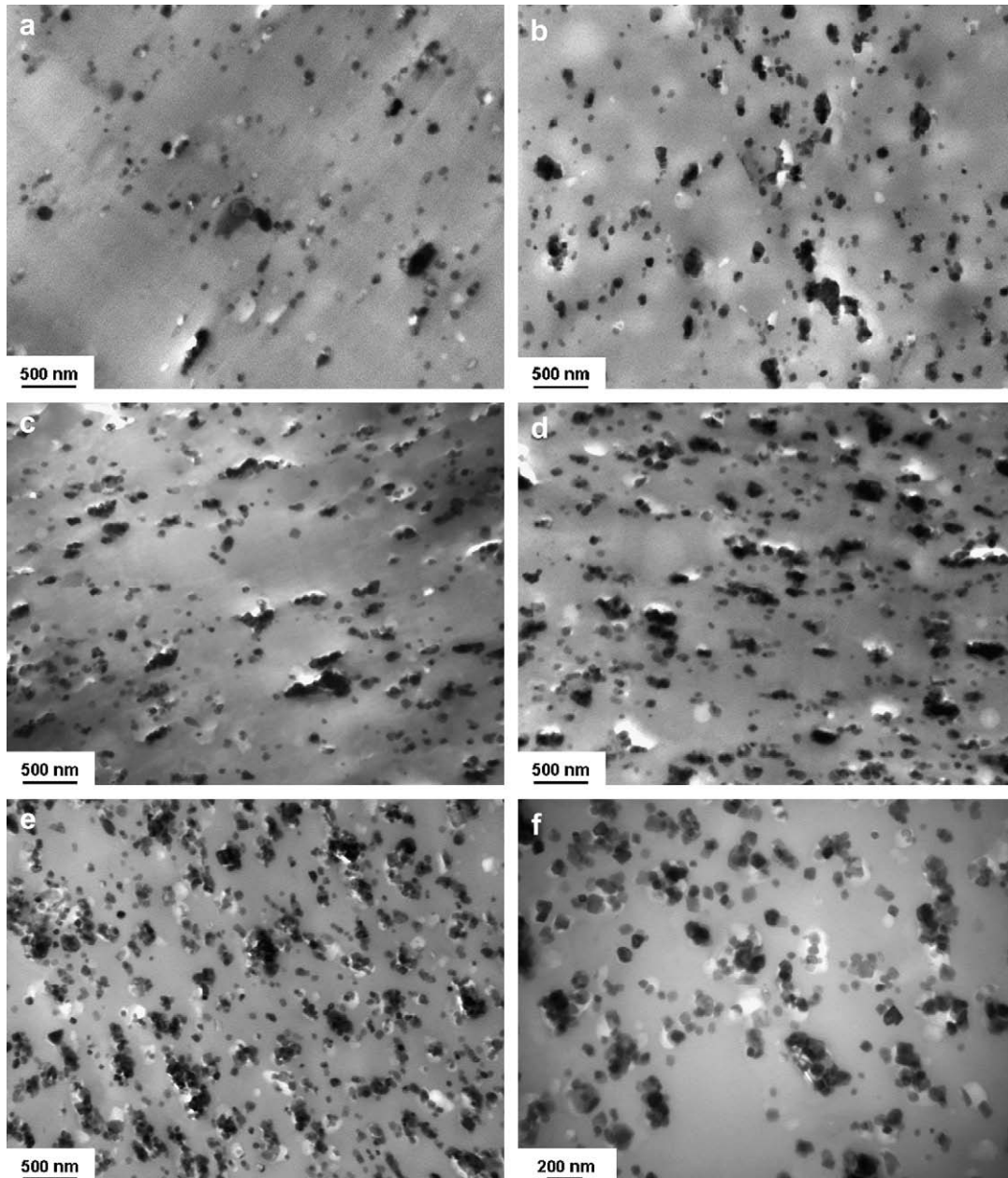
Fig. 6. TEM micrograph of PVC nanocomposite with (a) 3 phr, (b) 6 phr, (c) 9 phr, (d) 12 phr, (e) 20 phr NPCC, (f) higher magnification TEM micrograph of PVC nanocomposite with 20 phr nano-CaCO₃.

The effects of variation of particle spacing (d) and particle size on the evolution of the plastic zone in the composites were also studied by FEA simulation. Nanoparticle radii of 20, 30 and 40 nm were considered along with several values of d which correspond to 3, 6, 9, 12 and 20 phr nanoparticle fraction for simple cubic, BCC and FCC configurations.

Large displacement solving was carried out and the results analysed at each loading step. The loading step chosen was $\Delta U_y = 0.033$ nm; however, it was halved at small values of d in order to ensure convergence of the results. Plasticity was deemed to have been initiated when the von Mises stress in the matrix reached 59.5 MPa which first occurred adjacent to the nanoparticle. At higher loads, the distributions of the equivalent von Mises stress and strain were also analysed to ascertain the evolution of the shape and dimensions of the plastic zone.

The axisymmetric model considers that the matrix is in a cylindrical shape. A 3-dimensional FEA analysis where the particle lies in the centre of a cubical shape matrix was made to verify this assumption: for the purpose, one quarter of the hole and one quarter of its tributary volume were modeled. Two FEA simulations of a cubical matrix of $d = 50$ nm and $d = 23$ nm with a hole of 30 nm radius in the centre were made to confirm that the stress–strain behavior is similar to the FEA modeling with axisymmetric constraints. A free mesh of 3D solid linear elements, 8-node brick SOLID185 using enhanced strain formulation options was incorporated with symmetry boundary conditions applied on all planes except that with an applied displacement as illustrated in Fig. 4. The material model and the type of analysis match the conditions in the 2D axisymmetric model explained above.

3. Results and discussion

3.1. Composite microstructure

Fig. 5 shows a TEM micrograph of the calcium carbonate nanoparticles used to reinforce the PVC. The average particle size of the nano-CaCO$_3$ was found to be 60 ± 20 nm. The sample was found to have a surface area of 24 m^2/g using BET, which, assuming a spherical particle and density of 2.65 g/cm^3, gives an average particle size of 47 nm.

Fig. 6(a) shows a TEM micrograph of the PVC matrix with 3 phr nano-CaCO$_3$ where the filler appears to be distributed homogeneously within the polymer. Particle dispersion has been achieved by high levels of shear produced in the two-roll mill. Fig. 6(b–e) shows that particle agglomeration increases with increasing concentration of nano-CaCO$_3$ up to 12 phr. There are no obvious signs of delamination between the particle and matrix from the specimen preparation process.

Particle agglomeration is analysed using image analysis and results shown in Fig. 7. As all nano-CaCO$_3$ particles have the same size distribution when added to the mixture and assuming that no reaction between them takes place during processing, larger particles determined using image analysis are taken to be agglomerates. The fraction of dispersed particles gradually decreased with increasing particle volume fraction, showing increasing agglomeration.

3.2. Mechanical properties

The addition of nanoparticles led to a slight decrease in the tensile strength (Fig. 8). It is believed that rigid inorganic particles may promote localized yielding of the polymer matrix leading to void coalescence and fracture. The effect of the volume fraction of filler particle (ϕ_p) upon yield stress $\sigma_{c,y}$ of a particulate-filled composite has been explained by [28]:
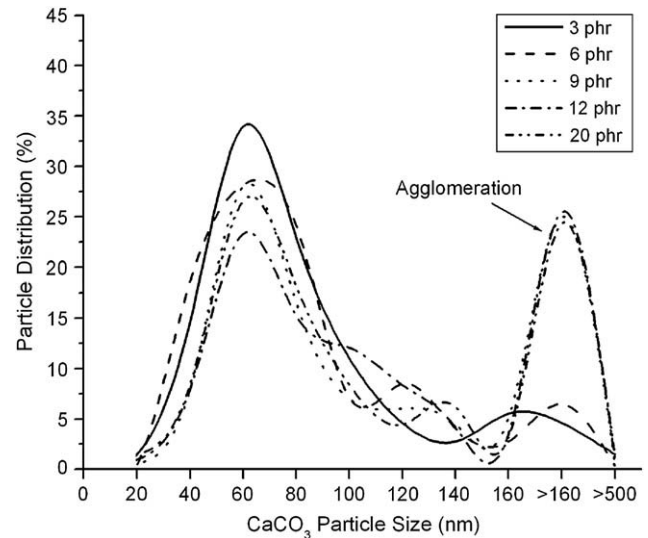

Fig. 7. Histogram of the particle size distribution from the TEM micrograph.

$$\sigma_{c,y} = \sigma_{m,y}\left(1 - \phi_p\right)\exp\frac{\beta\phi_p}{1 + 2.5\phi_p} \qquad (2)$$

where $\sigma_{m,y}$ is the yield stress of the matrix, β is an interfacial parameter describing the interaction of the matrix and nanoparticles, and was found to be 1.31 by fitting it to the experimental data. Similar results were reported by Sun et al. [29] who obtained a value of $\beta = 1.39$ for PVC reinforced with 80 nm CaCO$_3$ particles. The interfacial parameter β was found to increase with decreasing particle size [29]. Similarly, in this study the average particle size generally increases with volume fraction due to agglomeration and, thus, the composites with high particle volume fractions attend to lower β value which is represented by the lower tensile strength.

An alternative relationship commonly used for micron-sized rigid particles is given as Equation (3) [30]. However, when this is applied the correlation is poor, as shown in Fig. 8. Nakamura et al. [9] reported a slight decrease in tensile properties of PVC composites when reinforced with fine calcium carbonate particles
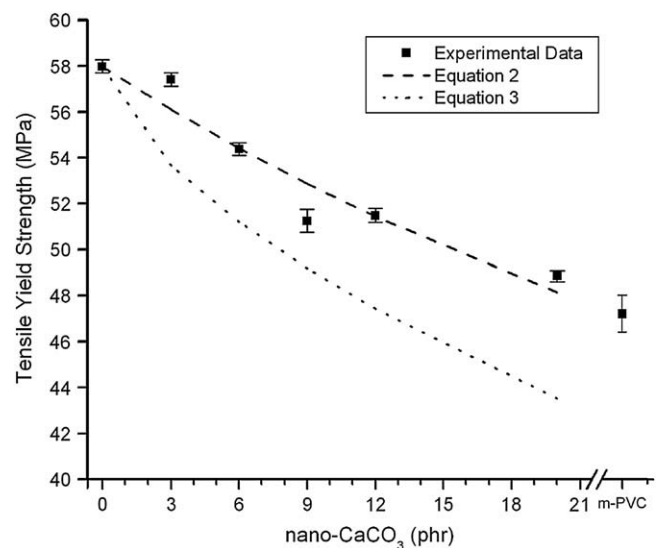

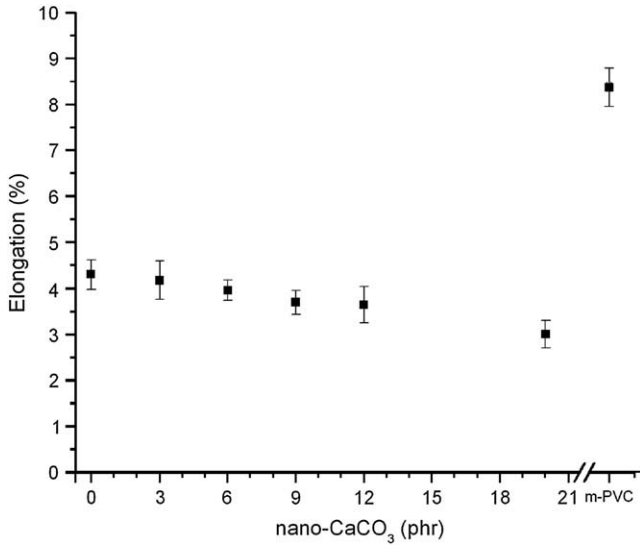**Fig. 8.** Effect of the nano-CaCO$_3$ content on the tensile strength of PVC nanocomposites.

Fig. 9. Effect of the nano-CaCO$_3$ content on the strain at break of PVC nanocomposites.

Fig. 11. Variation of storage modulus of PVC nanocomposites of different nano-CaCO$_3$ content with temperature.

(diameters between 0.4 and 0.6 μm), whereas PVC composites reinforced with larger calcium carbonate particles display a significant decrease in tensile strength.

$$\sigma_{c,y} = \sigma_{m,y}\left(1 - 1.21\phi_p^{2/3}\right) \tag{3}$$

It is hypothesized that the nanoparticles promote better particle–matrix phase bonding compared with the micron-sized particles due to the larger surface area, thus higher stress is required to form cavities [9]. Despite the decrease in yield strength with increasing filler loading, the yield stress of nanocomposites with 20 phr nano-CaCO$_3$ is still higher than the yield stress of the m-PVC with 6 phr CPE.

Tensile strain at break gradually decreased with increasing nano-CaCO$_3$ reinforcement, as shown in Fig. 9. Decrease in strain at break was also observed in PVC reinforced with micron-sized CaCO$_3$ particles [31] as the result of interfacial debonding. However, this contradicts the observation in recent work on PVC reinforced with nano-CaCO$_3$ particles [11,12], in which significant increases in
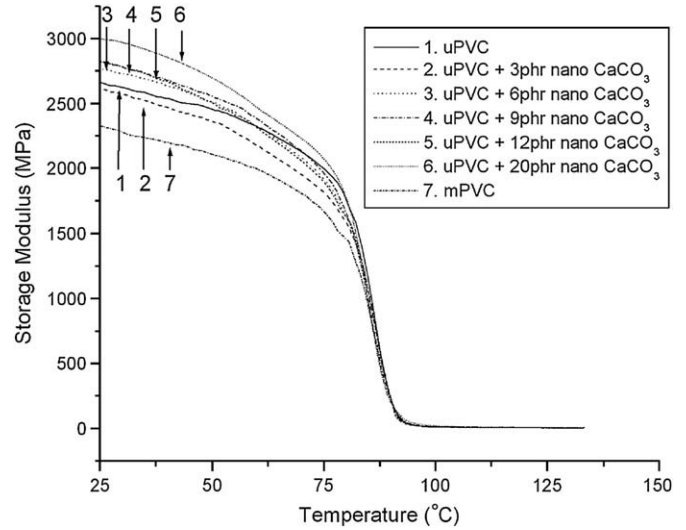
elongation at break was observed, which was attributed to ellipsoidal voids formation allowing ductile pull out [12]. This discrepancy may be attributed to different processing techniques and additives used in their study which resulted in a more ductile matrix with lower strength, delaying void coalescence.

Tensile testing showed that the nanoparticles increased the composites' stiffness as shown in Fig. 10. In addition, dynamic mechanical analysis (Fig. 11) also showed an increase in storage modulus with increasing fraction of calcium carbonate nanoparticulates below the glass transition temperature. Fig. 12 shows that ambient storage modulus at 25 °C increased with nanoparticulate fraction and was stiffer than monolithic PVC and m-PVC. A similar observation was made by Xie et al. [12] who recorded a stiffening effect due to the addition of nano-CaCO$_3$ particles in PVC matrix.

The increase in both Storage and Young's modulus, E, of the composite reinforced by the rigid inorganic particles can be described by the iso-stress rule of mixtures:
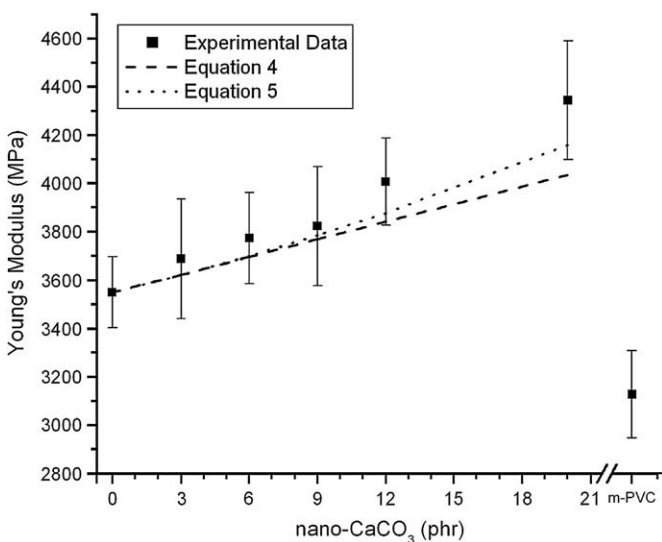

Fig. 10. Effect of the nano-CaCO$_3$ content on the Young's modulus of PVC nanocomposites.
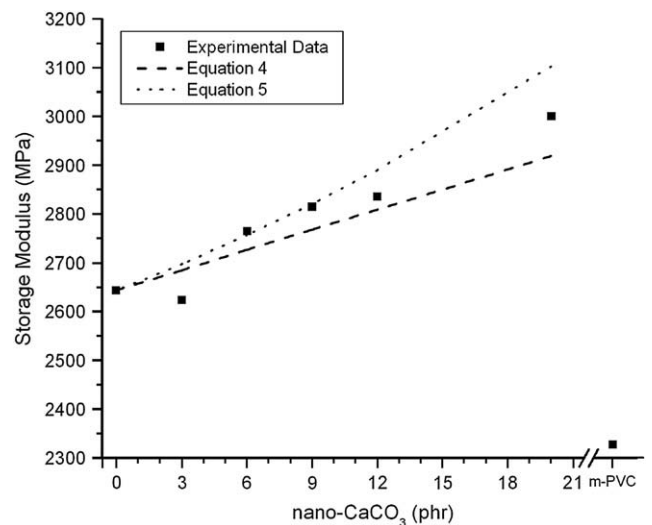

Fig. 12. Effect of the nano-CaCO$_3$ content on the storage modulus of PVC nanocomposites at 25 °C.
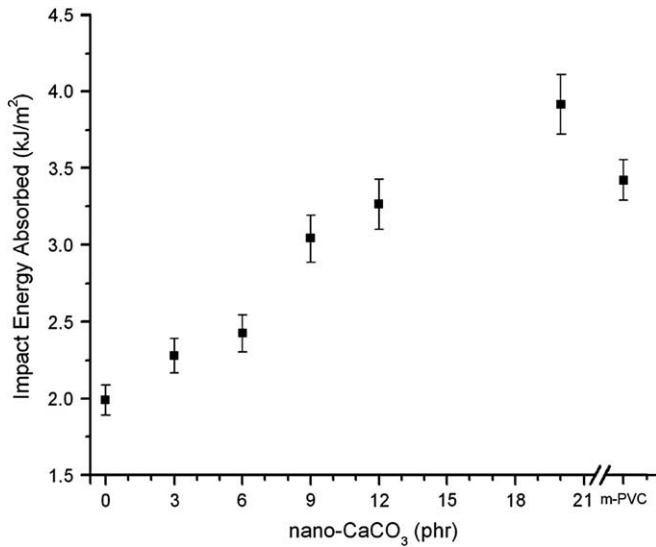
Fig. 13. Effect of the nano-CaCO₃ content on the Charpy impact energy per unit area of fracture surface of PVC nanocomposites.

$$E = \left(\frac{E_p E_m}{(1-\phi_p)E_p + \phi_p E_m} \right) \tag{4}$$

where ϕ the volume fraction and the subscripts p and m signify the particulate and matrix phases, respectively. Taking $E_p = 179$ GPa [32], and noting at $E_m = 3.56$ GPa, the predicted value of Young's modulus can be seen as the dashed line in Fig. 10. At higher volume fraction however, the increase in modulus exceeded that predicted by Equation (4). Differences between the predicted data and experimental data that could be due to the rule of mixture, which are more suitable for laminate structures than particulate-reinforced composites, do not account for particle size distribution. Alternatively, Nielsen's modified Kerner's equation for composite's Young's modulus accounts of the filler geometry and packing fraction as explained by [33,34]:

$$E_c = E_m \left(\frac{1 + AB\phi_p}{1 - B\psi\phi_p} \right) \tag{5}$$

where A is a constant dependent on the geometry of the filler phase and the Poisson's ratio of the matrix, B is a constant dependent on the relative stiffness of the particulate filler and the matrix and ψ is dependent on the packing fraction of the filler. Taking Poisson's ratio of the matrix to be 0.4 [35], A is calculated to be 1.25 and B is calculated to be close to 1 due to the high filler to matrix modulus ratio. Taking a packing fraction of 0.37 [36] for random close packing of the agglomerates, the value of the predicted modulus can be seen as the dotted line in Fig. 10.

The discrepancy between the rule of mixture and Nielsen's modified Kerner's equation arises as the rule of mixtures do not consider particle geometry, while generally the modulus increases as the particle decreases [33]. On the other hand, Nielsen's modified Kerner's equation considers individual particulate effect rather than the iso-stress conditions more appropriate to laminates. Furthermore, it takes into account the particle size distribution through the maximum packing fractions. When a packing fraction value of 0.37 for random close packing with agglomerates was adopted, the predicted Young's modulus data correlated well with the experimental data (Fig. 10). This agrees also with particle agglomeration at higher particle fractions as observed in the TEM micrographs (Fig. 6).
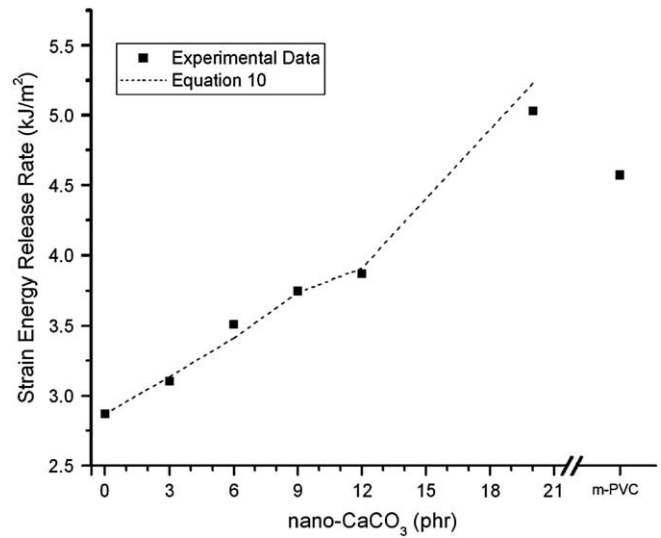

Fig. 14. Effect of nano-CaCO₃ content on the fracture toughness – expressed as strain energy release rate – of PVC nanocomposites.

Charpy impact energy shows a 95% increase with the introduction of 20 phr nanoparticles (Fig. 13) compared with unmodified PVC, and is higher than that of m-PVC. Similar results were also shown by Wu et al. [11]. Notably, the toughness enhancement as compared with the monolith is greater than that which has been achieved following the introduction of larger micron-sized CaCO₃ particles in which the addition of 20 phr by weight of 3 μm CaCO₃ into a rigid PVC pipe could achieve only a 53% increase in impact toughness [2,37–39]. This will be discussed later.

The strain energy release rate or toughness (G_c) is ascertained from the impact tests as described by the following equation [20]:

$$G = \frac{U_s}{TW} \cdot \left(\frac{dC}{C\, d\alpha} \right) = \frac{U_s}{TW\Phi(\alpha)} \tag{6}$$

where W is the specimen width, T the specimen thickness and U_s the impact energy absorbed. The calibration factor, $\Phi(\alpha)$ is a geometric term dependent upon compliance, C, and the ratio of crack length, over specimen width, $\alpha\ (=a/W)$, and calculated using the method of Plati and Williams [18]. Plotting the energy lost by the absorbed under impact loading, U_s is divided by the cross-
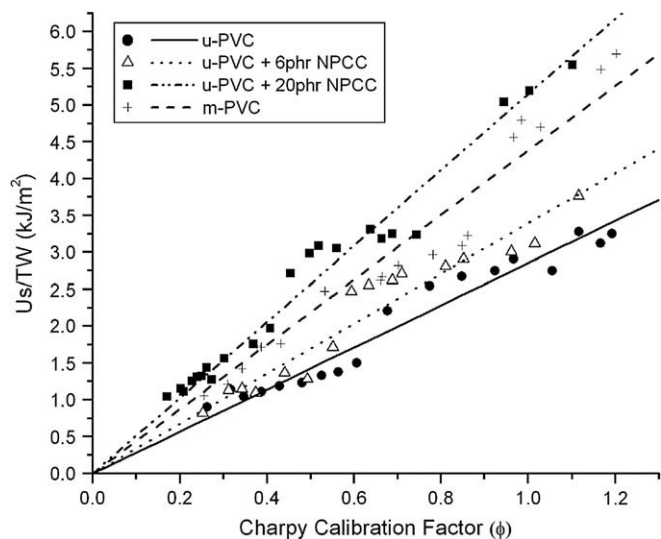

Fig. 15. Selected experimental results of strain energy release rate test.
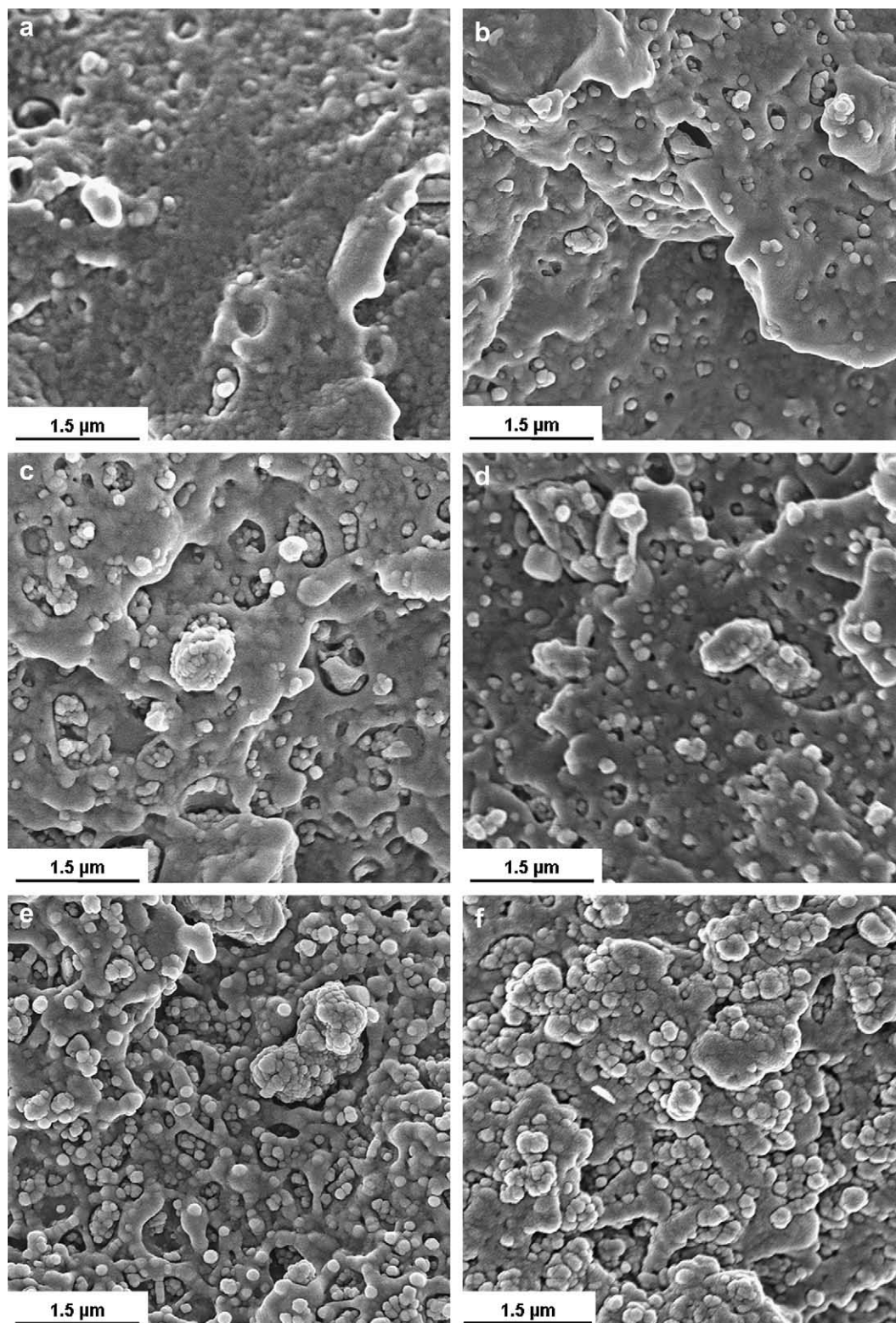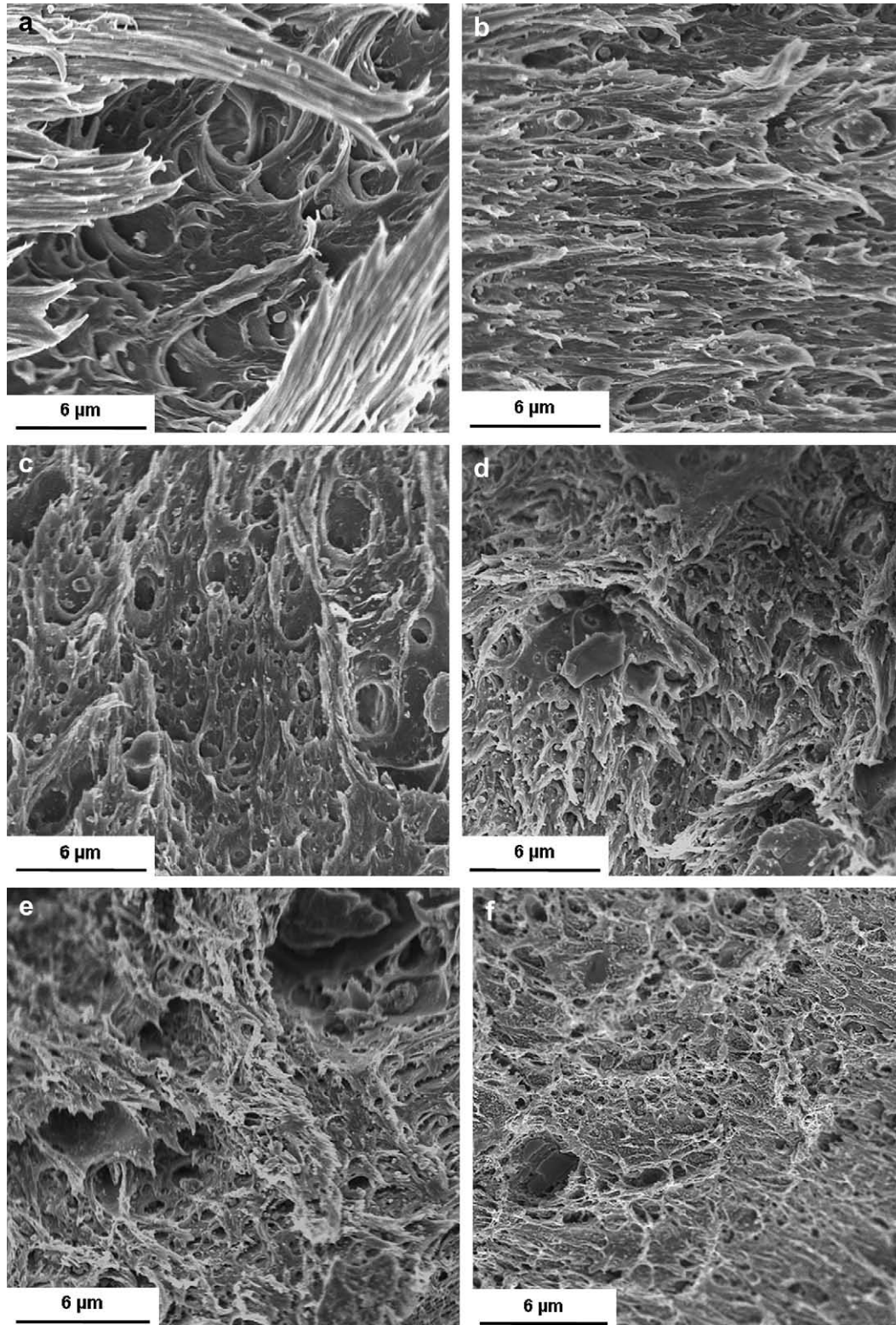
Fig. 16. FESEM micrographs of the impact fracture surface of (a) u-PVC, PVC with: (b) 3 phr, (c) 6 phr, (d) 9 phr, (e) 12 phr and (f) 20 phr nano-CaCO$_3$ content.

sectional area of the specimen TW, versus the calibration factor $\Phi(\alpha)$ producing a linear graph, the slope of which is G_c. The graph of G_c for increasing nanoparticle volume fractions is shown in Fig. 14. Equation (6) implies the line of best fit will pass through the origin, but there are other energy sinks – for example, the kinetic energy associated with movement of the specimen. In this work, it has

been assumed all the other energy losses are constant and the line of best fit is displaced vertically but otherwise unaltered. Selected results are shown in Fig. 15.

Fracture toughness (G_c), determined as described above, increased significantly with increasing fractions of nanoparticulate CaCO$_3$ filler (Fig. 14), from 2.89 kJ/m^2 for monolithic PVC to 5.03 kJ/m^2
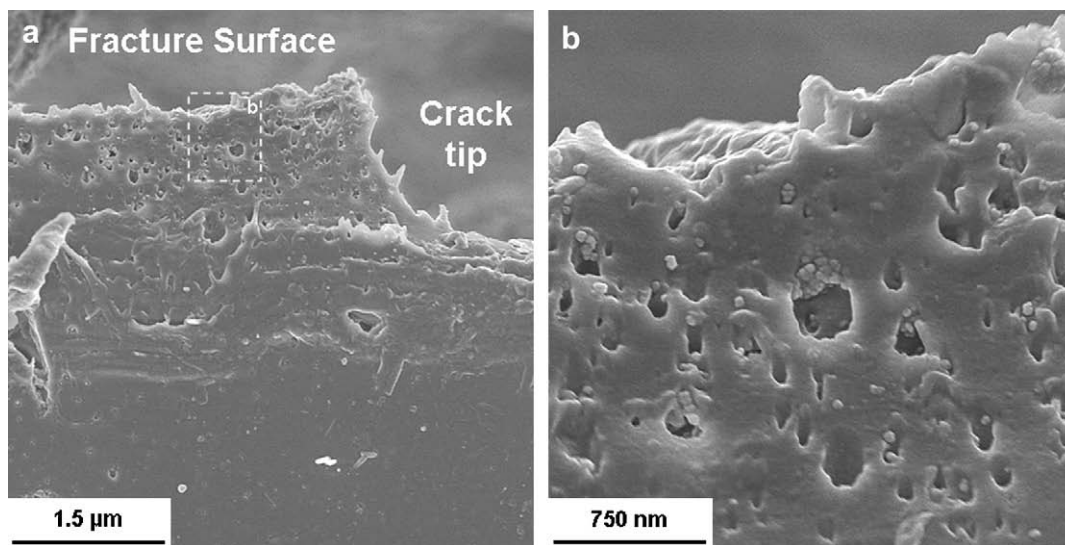
Fig. 17. FESEM micrographs of the tensile fracture surface of (a) u-PVC, PVC with: (b) 3 phr, (c) 6 phr, (d) 9 phr, (e) 12 phr and (f) 20 phr nano-CaCO₃ content.

for PVC with 20 phr nano-CaCO$_3$, slightly higher compare to m-PVC (4.79 kJ/m^2). The increasing fracture toughness corresponds with the impact test results shown in Fig. 13 but additionally provides a value of toughness which may be used in design. This further indicates also that the presence of nano-CaCO$_3$ particles can improve composite toughness.

3.3. Fracture surface observations

Impact fracture surface images show that the addition of nanoparticulate fillers alters the fracture behavior compared with unplasticized PVC (Fig. 16). While the latter shows a relatively smooth brittle fracture surface (Fig. 16(a)), nano-CaCO$_3$ particles

Fig. 18. FESEM micrographs of microtome cut cross-section of process zone of the impact fractured PVC nanocomposites with 9 phr nano-$CaCO_3$ content at (a) low magnification and (b) high magnification.

can be clearly seen on the fracture surface of the composites (Fig. 16(b–f)) and appear, in many cases, to be clearly debonded from the matrix. No such separation at the particle–matrix interface is seen in microstructural observations of the composites prior to mechanical testing (Fig. 6) indicating that debonding has occurred during the mechanical loading process. The formation of these voids around the particles is a result of their stress-concentrating effect. The scale and number of voids increased with nanofiller loading.

The fracture surface of unplasticized PVC following tensile testing shows a fibrous surface and extensive ductile deformation (Fig. 17(a)) compared with the smooth impact fracture surface (Fig. 16(a)). The addition of nanoparticles changes the fracture surface, with clearly observable cavities (Fig. 17(b–e)). The fibrous structure and number of voids increased with nanofiller loading which supports the proposal that cavity formation around the nanoparticles promotes yielding. This is consistent with the observations of several other workers who observed a large plastic deformation accompanied by a large number of voids on the fracture surface of PVC nanocomposites [11,12].

SEM analysis on the cross-section of a fracture surface shows cavitation close to the crack flanks in the fracture process and wake zones with the extent of cavitation decreasing as one moves away from the fracture plane (Fig. 18(a)). A higher magnification image of the near crack-tip plastic zone (Fig. 18(b)) shows the presence of filler particles in each cavity. This further confirms a deformation mechanism where cavitation occurs within the crack-tip process zone.

3.4. Finite element analysis

The purpose of the model is to explain the experimentally-observed effect of the addition of a nanoparticle phase upon mechanical behavior in terms of microstructural deformation processes. The contour plots of von Mises stress at different applied tensile strains show that stress evolves as an elliptical shell around the particles (Fig. 19(a–c)). Fig. 20(a–c) shows the contours of von Mises strain with shapes similar to the equivalent stress. Plastic deformation is initiated at the side of the particles, and eventually encapsulated the whole particle as shown in Fig. 20.

Furthermore, the von Mises stress at the onset of plastic deformation in the matrix (at the edge of the particles) increases with the normalized inter-particle distance ($2d/r_p$) (Fig. 21). This implies that the stress at the beginning of plasticity decreased with increasing particle volume fractions, indicating that inter-particle proximity affects the stress field and therefore the yield point of the composite. This corresponds to the decrease of the experimental value of tensile yield strength with increasing particle volume fraction and size and supports the hypothesis that weakly bonded nanoparticles promote matrix yielding due to the enhanced cavity formation as seen in the tensile fracture surfaces in Fig. 17.

A 3-dimensional FEA analysis was also performed to ascertain the compatibility between the axisymmetrical model, assuming a cylindrical matrix, and the cube-shaped matrix. Fig. 22 describes the 3D contour plot of the von Mises equivalent stress (Fig. 22(a)) and strain (Fig. 22(b)), for particles spacing $d = 50$ nm and particle radius of $r_p = 30$ nm at $\varepsilon_c = 2\%$ applied tensile strain. It is clear that the distribution of the equivalent stress is similar to the one in the axisymmetric model, in which the high stress level is in an elliptical shape around the particles and the low stress region is above the particles. Fig. 22(a) also shows the area above the particles which is not affected by the neighboring particles. This confirmed the validity of the axisymmetric constraint to model the stress–strain behavior of the hole in the matrix.

From the stress–strain curve of the monolithic matrix (Fig. 3), the onset of plasticity occurs at a tensile stress of $\sigma_{m,y} = 59.5$ MPa and at a tensile strain of approximately $\varepsilon_{m,y}^p = 2\%$. We then ascertain the geometry of the plastic zone around the particles by considering a contour plot of the von Mises equivalent strain – for example, in Fig. 20(b–c), the grey area represents an equivalent plastic strain ($\varepsilon_m^{eqv,p}$) of greater than 2%. The dimensions of the elliptical plastic zone at applied tensile stress and strain of $\sigma_c = 102$ MPa and $\varepsilon_c = 2\%$, respectively, are plotted in Fig. 23 for different inter-particle distances where r_h is the horizontal radius and r_v is the vertical radius of the ellipsoidal plastic zone. Fig. 23 also shows that the ratio of the volume of the plastic zone ($V_{in} = 4\pi r_h^2 r_v/3$) over the volume of the particle ($V_p = 4\pi r_p^3/3$) – represented as V_{in}/V_p – increases with increasing $2d/r_p$. The increase in the plastic zone size with increasing inter-particle spacing (d) indicates that the particles proximity affects the plastic zone size by limiting its growth.

The variation of the particle radius r_p for a certain volume fractions did not change the dimensions of the plastic zone with respect to the particle radius (i.e., the ratio of r_h/r_p and r_v/r_p). However the plastic zone is significantly influenced by the inter-

3.5. Fracture mechanism

The toughening of PVC by a micron-sized $CaCO_3$ phase has been explained by the crack-front bowing mechanism in which the particles act as a barrier for crack growth [13]. In thermosetting systems, which generally have higher resistance to plastic
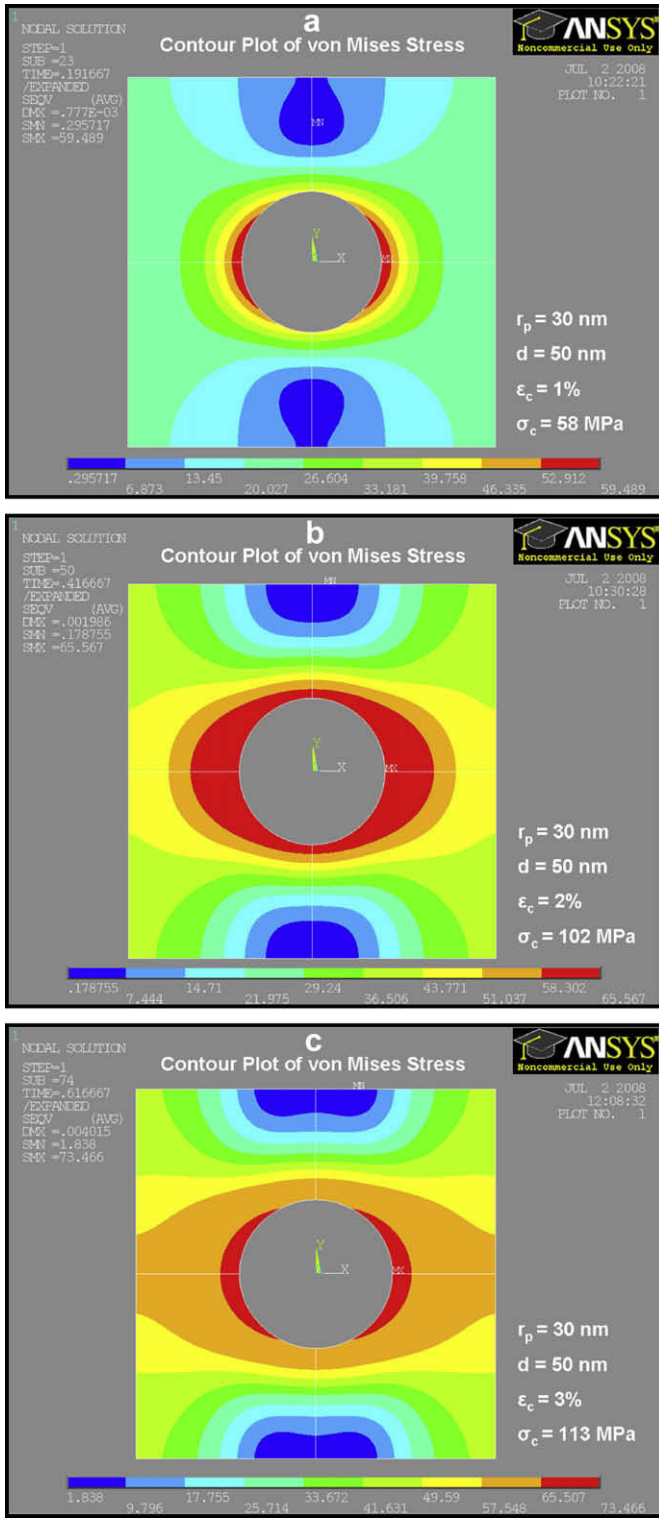

Fig. 19. Evolution of the von Mises stress contour plot for $r_p = 30$ nm and $d = 50$ nm ($2d/r_p = 3.33$) at an applied nominal tensile strain and stress of: (a) $\varepsilon_c = 1\%$ and $\sigma_c = 58$ MPa, (b) $\varepsilon_c = 2\%$ and $\sigma_c = 102$ MPa, (c) $\varepsilon_c = 3\%$ and $\sigma_c = 113$ MPa.

particle spacing and thus, the ratio between the particles spacing and particles radius ($2d/r_p$). In the case of rubber reinforced polymer, Wu [27] showed that the toughness improvement is more influenced by the inter-particle distance (ligament thickness) rather than by particle size, consistent with our observations of weakly bonded stiff particles.
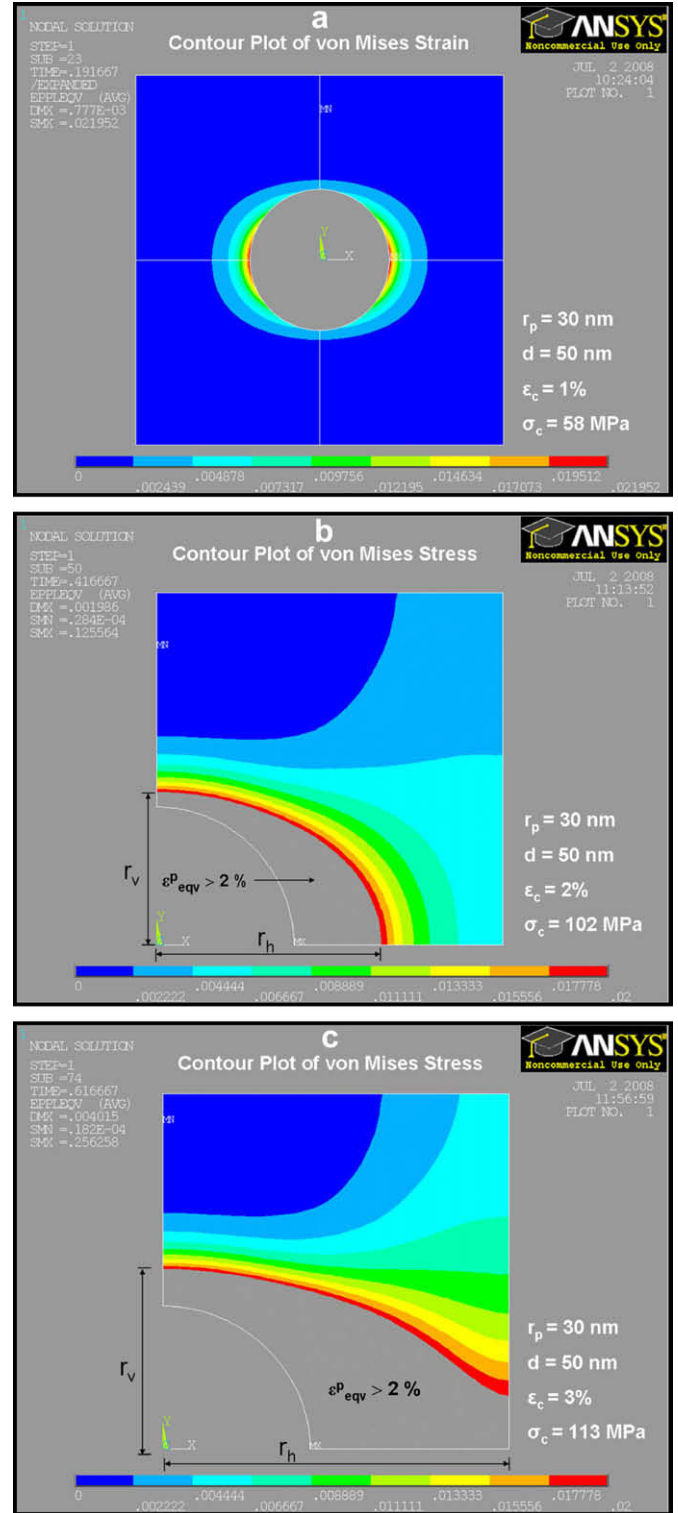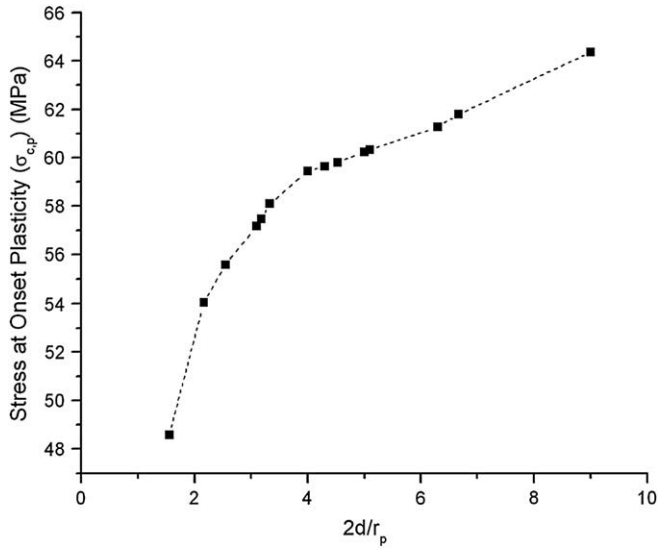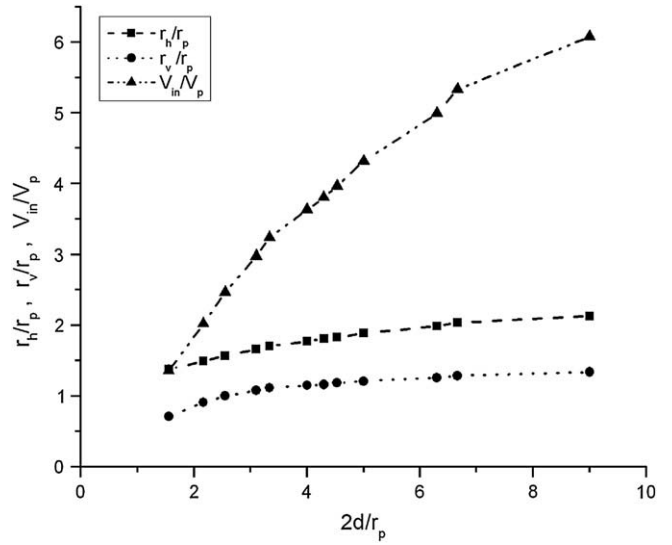

Fig. 20. Evolution of the von Mises strain contour plot for $r_p = 30$ nm and $d = 50$ nm ($2d/r_p = 3.33$) at an applied nominal tensile strain and an stress of (a) $\varepsilon_c = 1\%$ and $\sigma_c = 58$ MPa, (b) $\varepsilon_c = 2\%$ and $\sigma_c = 102$ MPa, (c) $\varepsilon_c = 3\%$ and $\sigma_c = 113$ MPa.

Fig. 21. Variation of von Mises equivalent stress at the onset of plastic deformation according to FEA with normalized inter-particle distance.

Fig. 23. Normalized plastic zone dimensions in horizontal (r_h/r_p) and vertical direction (r_v/r_p), and the corresponding volume of plastic deformation around the particles as a function of normalized inter-particle distance ($2d/r_p$) measured at $\sigma_c = 101.86$ MPa and $\varepsilon_c = 2\%$.
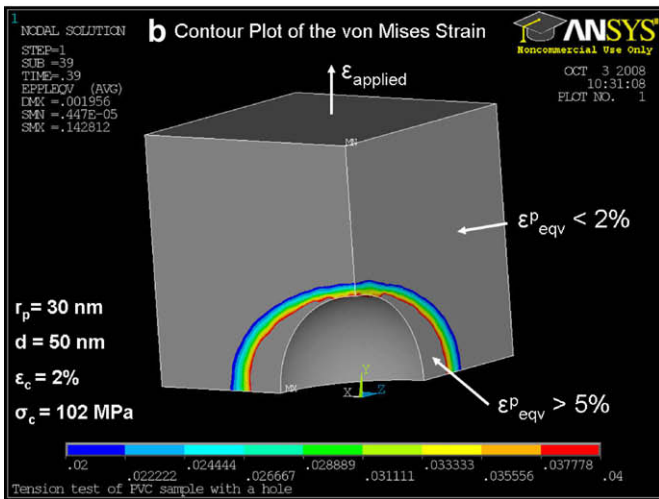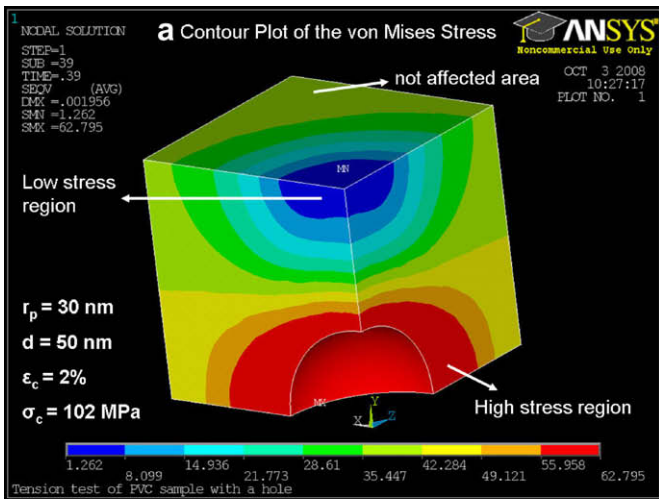
Fig. 22. 3D contour plot of the von Mises equivalent (a) stress and (b) strain for FEA model of $r_p = 30$ nm and $d = 50$ nm and at an applied nominal tensile strain and stress of 2% and 102 MPa, respectively. The contour plot of the von Mises stress (a) also shows the area above the particle which is not affected by the neighboring particles, thus confirming the validity of axisymmetric FEA model.

deformation, SEM micrographs have shown the possibility of crack pinning by rigid nano-sized particles [40]; but this is not observed in thermoplastics such as PVC. Instead, observations of the fracture surface and crack process zone indicate that in the case of nanometer-sized inclusions, the filler particles act as nucleation sites for cavitation. This cavitation precipitates localized plastic deformation through the release of mechanical plastic constraint [11] increasing the size of the crack-tip process zone and, thus, the work required for crack propagation.

A further difference between micron- and nanometer-sized fillers is that the former are sufficiently large to initiate Griffith-type cracking whereas the latter are comparable in size with polymer substructures in PVC [41] and, therefore, promote plastic deformation rather than initiate fracture.

The overall increase in toughness depends on the size of the process zone and the number of debonded particles, which can be calculated based on the height of the process zone (h), particle volume fraction (ϕ_p) and particle radius (r_p). Thus, the number of particles debonded per unit area (N_p) is the product of the span of process zone, both above and below the fracture plane ($2h$), and the volume fraction of the particles, divided by the particle volume. The height of the process zone itself can be measured or calculated by an Irwin approach. Thus the number of particles debonded per unit area (assuming unit thickness) can be expressed as [42]:

$$N_p = \frac{3h\phi_p}{2\pi r_p^3} \tag{7}$$

The energy needed to break the particle–matrix bond will contribute to the overall increase in toughness, and the interfacial fracture energy per unit area is estimated using [42,43]:

$$G_{ic,i} = \frac{3\sigma_{max}^2 r_p}{4\pi E_m} \tag{8}$$

where E_m is the matrix modulus and r_p is the particle radius. σ_{max} is the debonding strength which is set to be the strength at which inelastic deformation was initiated according to the tensile test curve [43], i.e., the yield point of the PVC matrix which occur at $\varepsilon_{m,y}^p = 2\%$ plastic strain (Fig. 3).

The energy required to inelastically deform the matrix around each particle per unit volume (W_{in}) can be estimated from the area of plasticity underneath the stress–strain curve of the matrix at 2% offset strain which in this case is 1225 kJ/m^3 [43]. The deformed volume (V_{in}) is assumed to occur in an ellipsoidal shell around the debonded particles, with a horizontal radius (r_h) and vertical radius (r_v) as shown in Fig. 20.

Thus the increase in fracture energy of the PVC nanocomposite system can be predicted by multiplying the sum of the interfacial fracture energy and the inelastic deformation energy with the number of particles per unit area in the process zone [43]:

$$G_{ic,c} = (1 - \phi_f)G_{ic,m} + \left(\frac{3h\phi_p}{2\pi r_p^3}\right)$$
$$\left(4\pi r_p^2 G_{ic,i} + \frac{4}{3}\pi\left(ab^2 r_p^3 - r_p^3\right)W_{in}\right) \quad (9)$$

where r_p is the particle radius and $a = r_v/r_p$ and $b = r_h/r_p$ as plotted in Fig. 23. When Equation (8) is substituted into Equation (9), the fracture toughness prediction thus becomes:

$$G_{ic,c} = (1 - \phi_f)G_{ic,m} + \left(\frac{3h\phi_p}{2\pi}\right)\left(\frac{3\sigma_{max}^2}{E_m} + \frac{4}{3}\pi\left(ab^2 - 1\right)W_{in}\right) \quad (10)$$

If the inter-particle distances are calculated using Equation (1), assuming an FCC configuration the predicted strain energy release rate (G_c) is in good agreement with the experimental data, as indicated in Fig. 14. If the particle distances are calculated assuming a simple cubic structure, the G_c prediction does not conform to the experimental results. This is because the simple cubic spacing represents a smaller inter-particle distance when compared with the FCC spacing. Particle agglomerations as observed in the TEM micrographs (Fig. 6) create an uneven particle size distribution, which increases the inter-particle distance. Thus the FCC spacing assumption is more suitable in this case.

Substituting these parameters into Equation (10), leads to an increase of only 10–13.5% in fracture toughness depending on the nanoparticle volume fraction of the composites (the lower and higher value corresponds to 3 phr and 20 phr of nano-CaCO$_3$ reinforcement, respectively). Therefore, the main contributor to the increase in fracture energy appears to be matrix deformation around the particles that enhances plastic zone formation at the crack-tip.

Equation (10) also indicates that the increase of G_c, based on the cavitation toughening mechanism, is independent of particle radius but dependent on the volume fractions of the particles and the inter-particle distance. However, it must be noted that the significance of the nano-sized particles is their effectiveness in providing cavity nucleation sites, whereas larger micro-sized particles can act as stress concentrators, initiating premature fracture initiation. A similar conclusion was made by Cotterell et al. [15].

Mechanical testing data suggest that at 20 phr nano-CaCO$_3$ reinforcement, the fracture toughness, modulus and strength are higher than the m-PVC with 6 phr of CPE impact modifier. Nevertheless, fracture surface observation shows that the nanocomposites fail in a brittle manner at high loading rate. Thus, careful consideration must be taken when incorporating nanoparticles in PVC for high pressure pipe applications.

4. Conclusions

The mechanical deformation and fracture behavior of PVC nanocomposites with nanometer-sized calcium carbonate particle filler has been studied to ascertain the effect of the filler upon microstructural processes. Experimental results showed that:

1. The two-roll mill could produce PVC/nano-CaCO$_3$ composites with homogeneous particles dispersion. The particles tend to agglomerate with increasing nano-CaCO$_3$ particles fractions.
2. Increasing filler content leads to increases in impact energy toughness and modulus, but a slight decrease in tensile strength.
3. Increased stiffness may be explained by analytical mechanics relationships and appears unrelated to changes in the elastic deformation of the matrix.
4. Nano-sized rigid inorganic particles reinforcement at 20 phr provides a PVC material with higher toughness and stiffness and slightly higher tensile strength when compared to m-PVC with 6 phr of CPE.

Analysis of the fracture surfaces and process zone, coupled with a model of deformation, revealed that:

5. With weak particle–matrix bonding, plastic deformation initiates in the vicinity of the inclusion.
6. The magnitude of the applied stress to initiate plastic deformation depends on the presence and distance to the neighboring particles.
7. The plastic deformation zone around the spherical inclusion is elliptical in shape and size is proportional to the particle radius and affected by the presence and distance to the neighboring particles.
8. Increases in toughness and impact energy may be attributed to enhanced micro-void formation initiated by nanoparticles, which locally deform the matrix surrounding the particles and initiate mass plastic deformation.
9. Within the crack process zone, cavities are associated with the nano-CaCO$_3$ particles, and in the absence of crazes, cavitation is the dominant form of plastic deformation which provides toughness enhancement. However, the enhanced cavity formation also promotes matrix's yielding, which leads to a reduction in tensile strength and strain at break.

References

[1] Voet A. J Polym Sci Part D Macromol Rev 1980;15(1):327–73.
[2] Katz HS, Milewski JV. Handbook of fillers for plastics. Springer; 1987.
[3] Titow WV. PVC technology. 4th ed.; 1984.
[4] Sumita M, Tsukihi H, Miyasaka K, Ishikawa K. J Appl Polym Sci 1984;29(5):1523–30.
[5] Sumita M, Tsukumo Y, Miyasaka K, Ishikawa K. J Mater Sci 1983;18(6):1758–64.
[6] Sumita M, Shizuma T, Miyasaka K, Ishikawa K. J Macromol Sci Part B Phys 1983;22(4):601–18.
[7] Jiang L, Lam YC, Tam KC, Chua TH, Sim GW, Ang LS. Polymer 2005;46(1):243–52.
[8] Bucknall CB, Paul DR. Polymer blends. John Wiley & Sons; 2000.
[9] Nakamura Y, Fukuoka Y, Iida T. J Appl Polym Sci 1998;70:311–6.

[10] Mishra S, Perumal GB, Naik JB. Polym Plast Technol Eng 1997;36(4):489–500.
[11] Wu DZ, Wang XD, Song YZ, Jin RG. J Appl Polym Sci 2004;92(4):2714–23.
[12] Xie XL, Liu QX, Li RKY, Zhou XP, Zhang QX, Yu ZZ, et al. Polymer 2004;45(19): 6665–73.
[13] Lange FF, Radford KC. J Mater Sci 1971;6(9):1197–203.
[14] Faber KT, Evans AG. Acta Metall 1983;31:565–76.
[15] Cotterell B, Chia JYH, Hbaieb K. Eng Fract Mech 2007;74(7):1054–78.
[16] Marshall GP, Williams JG, Turner CE. J Mater Sci 1973;8(7):949–56.
[17] Brown HR. J Mater Sci 1973;8(7):941–8.
[18] Plati E, Williams JG. Polym Eng Sci 1975;15(6):470–7.
[19] WRc water industry specification no. 4-31-06 issue 1: specification for blue unplasticised PVC pressure pipes ijap-fbfcpwuu.
[20] Pavan A. ESIS publication 28. In: Moore DR, Pavan A, Williams JG, editors. Fracture mechanics testing methods for polymer adhesives and composites. Amsterdam: Elsevier Science; 2001.
[21] Whittle AJ, Burford RP, Hoffman MJ. Plast Rubber Compos 2001;30(9):434–40.
[22] ISO R527:1966, Plastic – determination of tensile properties.
[23] AS1145.1-2001, Determination of tensile properties of plastic materials.
[24] ISO/DIS 11673.2:1999. Determination of the fracture toughness properties of unplasticized poly(vinyl chloride) (PVC–U) pipes; 1999.
[25] AS1146.2-1990, Methods for impact tests on plastics – Charpy impact resistance.
[26] Du XW, Sun G, Nie C. Key Eng Mater 2004;274:1077–82.
[27] Wu S. J Appl Polym Sci 1988;35(2):549–61.
[28] Vörös G, Fekete E, Pukánszky B. J Adhes 1997;64(1):229–50.
[29] Sun S, Li C, Zhang L, Du HL, Burnell-Gray JS. Polym Int 2006;55:158–64.
[30] Nicolais LNM. Polym Eng Sci 1971;11(3).
[31] Nakamura Y, Azuma F, Iida T. Polym Polym Compos 1998;6(1):7–13.
[32] Kelly A, Zweben C. Comprehensive composite materials. Amsterdam; New York: Elsevier; 2000.
[33] Lewis T, Nielsen L. J Appl Polym Sci 1970;14:1449–71.
[34] Nielsen LE. J Polym Sci Part B Polym Phys 1979;17(11):1897–901.
[35] Erhard G. Designing with plastics. Hanser Publishers; 2006.
[36] Vassileva E, Friedrich K. J Appl Polym Sci 2003;89(14):3774–85.
[37] Zuiderduin WCJ, Westzaan C, Huetink J, Gaymans RJ. Polymer 2003;44(1): 261–75.
[38] Lee J, Yee AF. Polymer 2001;42(2):577–88.
[39] Lee J, Yee AF. Polymer 2001;42(2):589–97.
[40] Wetzel B, Rosso P, Haupert F, Friedrich K. Eng Fract Mech 2006;73(16F): 2375–98.
[41] Burgess RH. Manufacture and processing of PVC. UK: Spon E&FN; 1982.
[42] Gent AN. J Mater Sci 1980;15(11):2884–8.
[43] Norman DA, Robertson RE. Polymer 2003;44(8):2351–62.